

Quantum dynamics of Mn^{2+} in dimethylammonium magnesium formate

Cite as: J. Chem. Phys. **154**, 154201 (2021); <https://doi.org/10.1063/5.0046984>

Submitted: 09 February 2021 • Accepted: 01 April 2021 • Published Online: 16 April 2021

 M. Orio,  J. K. Bindra, J. van Tol, et al.

COLLECTIONS

Paper published as part of the special topic on [Special Collection in Honor of Women in Chemical Physics and Physical Chemistry](#)



View Online



Export Citation



CrossMark

ARTICLES YOU MAY BE INTERESTED IN

[Layer and spontaneous polarizations in perovskite oxides and their interplay in multiferroic bismuth ferrite](#)

The Journal of Chemical Physics **154**, 154702 (2021); <https://doi.org/10.1063/5.0046061>

[Phase separation in mixed suspensions of bacteria and nonadsorbing polymers](#)

The Journal of Chemical Physics **154**, 151101 (2021); <https://doi.org/10.1063/5.0045435>

[Time-reversible and norm-conserving high-order integrators for the nonlinear time-dependent Schrödinger equation: Application to local control theory](#)

The Journal of Chemical Physics **154**, 154106 (2021); <https://doi.org/10.1063/5.0050071>

The Journal
of Chemical Physics

SPECIAL TOPIC: Low-Dimensional
Materials for Quantum Information Science

Submit Today!



Quantum dynamics of Mn^{2+} in dimethylammonium magnesium formate

Cite as: J. Chem. Phys. 154, 154201 (2021); doi: 10.1063/5.0046984

Submitted: 9 February 2021 • Accepted: 1 April 2021 •

Published Online: 16 April 2021



View Online



Export Citation



CrossMark

M. Orio,^{1,a)} J. K. Bindra,^{2,3} J. van Tol,³ M. Giorgi,⁴ N. S. Dalal,^{2,3} and S. Bertaina^{5,b)}

AFFILIATIONS

¹CNRS, Aix-Marseille Université, Centrale Marseille, iSm2, Institut des Sciences Moléculaires de Marseille, Marseille, France

²Department of Chemistry, Florida State University, Tallahassee, Florida 32310, USA

³The National High Magnetic Field Laboratory, Tallahassee, Florida 32310, USA

⁴Aix Marseille Université, CNRS, Centrale Marseille, FSCM, Spectropole, Marseille, France

⁵CNRS, Aix-Marseille Université, IM2NP (UMR 7334), Institut Matériaux Microélectronique et Nanosciences de Provence, Marseille, France

Note: This paper is part of the JCP Special Collection in Honor of Women in Chemical Physics and Physical Chemistry.

^{a)} Author to whom correspondence should be addressed: maylis.orio@univ-amu.fr

^{b)} Electronic mail: sylvain.bertaina@im2np.fr

ABSTRACT

Dimethylammonium magnesium formate, $[(\text{CH}_3)_2\text{NH}_2][\text{Mg}(\text{HCOO})_3]$ or DMAMgF, is a model used to study high temperature hybrid perovskite-like dielectrics. This compound displays an order–disorder phase transition at about 260 K. Using multifrequency electron spin resonance in continuous wave and pulsed modes, we herein present the quantum dynamics of the Mn^{2+} ion probe in DMAMgF. In the high temperature paraelectric phase, we observe a large distribution of the zero field splitting that is attributed to the high local disorder and further supported by density functional theory computations. In the low temperature ferroelastic phase, a single structure phase is detected and shown to contain two magnetic structures. The complex electron paramagnetic resonance signals were identified by means of the Rabi oscillation method combined with the crystal field kernel density estimation.

Published under license by AIP Publishing. <https://doi.org/10.1063/5.0046984>

I. INTRODUCTION

Metal–organic frameworks (MOFs) are constituted of two main building units: the framework consisting of metal centers connected to each other by organic linker molecules. Previous works have reported hybrid MOFs such as $[(\text{CH}_3)_2\text{NH}_2][\text{M}(\text{HCOO})_3]$ (dimethylammonium metal formate or DMAMF), with M being divalent transition metal ions^{1–7} and DMA being the cation molecule in the cavity whose dynamics are responsible for the dielectric transition.

Heat capacity and dielectric measurements of DMZnF indicated a phase transition at ~ 160 K.² The order–disorder phase transition is a common property in these materials. At higher temperatures in the disordered phase, the $(\text{CH}_3)_2\text{NH}_2^+$ cation (DMA⁺, dimethylammonium) that is trapped within the cage is disordered, which means that the nitrogen from the amine group can occupy

three locally equivalent positions by forming hydrogen bonds with oxygen atoms from the formate linkers. As the temperature is decreased, the long-range order is established due to the cooperative ordering of the cations at T_c . In the low temperature phase, the nitrogen atoms freeze into a single position in the cavity, while the metal–formate framework becomes more distorted.² The Mg analog (DMMgF) is known to exhibit dielectric transitions at exceptionally high T_c of ~ 270 K.⁸ The single crystal x-ray diffraction (XRD) studies reveal that the high- and low-temperature phases of these compounds belong to the trigonal, $R\bar{3}c$ (centrosymmetric), and the monoclinic, Cc (non-centrosymmetric), space groups, respectively.^{8,9} The metal–formate frameworks of these materials consist of pseudo-cuboid cavities, each containing a single DMA⁺ cation, as shown in Fig. 1. DMMgF has been intensively investigated using heat capacity, dielectric, and XRD measurements.^{8–10} However, despite these huge efforts, the precise nature of the phase

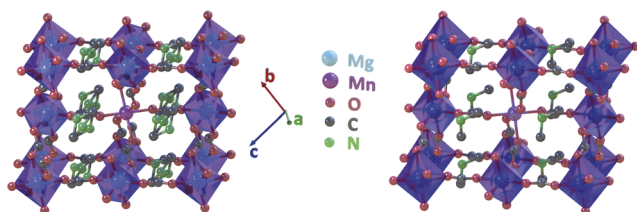


FIG. 1. Crystal structure of the DMAMgF framework at $T > T_c$ (left, HT phase— $R\bar{3}c$) and $T < T_c$ (right, LT phase— Cc). The Mg (blue spheres) and Mn probes (pink spheres) are in the center of the oxygen octahedron. The DMA⁺ cations are located in the formate cages and have three equivalent positions in the HT phase, which are represented by three nitrogen atoms (green spheres), while in the LT phase, only one position is expected. For clarity, the hydrogen atoms are not shown. The figures are realized with Blender (3D open source software: <https://www.blender.org/>) using the structure investigated in this work.

transition in DMAMgF is still obscure. Among many other experimental methods, electron paramagnetic resonance (EPR) spectroscopy is well-suited to study structural phase transitions.^{4,5,11–14} It is used to detect the local environment of a paramagnetic center (e.g., local order parameter such as electric polarization) that can be influenced by structural transformations. Although most of the MOFs do not contain any intrinsic paramagnetic center, they can be doped with a small amount of paramagnetic transition metal ions (e.g., Mn²⁺), which act as local probes in the structure. In our previous studies, we have employed continuous wave (CW) EPR spectroscopy to successfully investigate the phase transition in undoped DMAMnF and DMAZnF:Mn²⁺ MOFs.^{4,5} However, due to the strong magnetic dipolar and exchange interactions between the Mn²⁺ centers, the EPR spectrum of DMAMnF consists of a single broad line, which is barely sensitive to the ordering of DMA⁺ cations.⁴ In addition, the slow dynamics of the DMA⁺ cation around the phase transitions in DMAZnF:Mn²⁺ were investigated using S-band EPR (4 GHz). S-band EPR spectra yielded clear signatures of the slow motion of both the formate and DMA⁺ groups.⁵

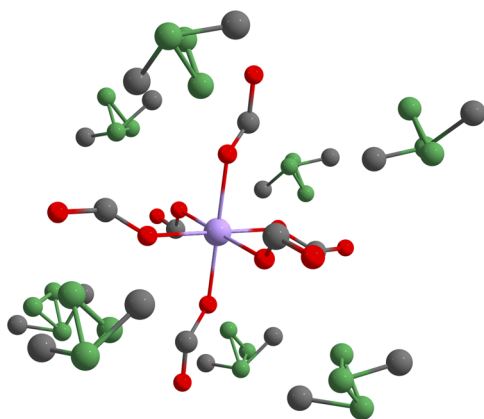


FIG. 2. Minimal model used for computing the ZFS parameters in DMAMgF showing equivalent positions of the nitrogen atoms in the DMA⁺ cations. Color code: Mn, pink spheres; N, green spheres; O, red spheres; C, dark gray spheres; and H is omitted for clarity.

EPR methods have also been used to characterize the low temperature phases and dynamics in Mn²⁺ and Cu²⁺ doped niccolite [NH₃(CH₂)₄NH₃][Zn(HCOO)₃]₂.¹⁵ Mn²⁺ doping in such systems is the probe of choice for the local properties (crystal fields and motion). The large number of EPR transitions as well as the long coherence time allows us to have access to the quantum dynamics of the spins. Large spin ions, such as Mn²⁺ ($S = 5/2$), are used for their quantum coherence properties as a potential qubit.^{16,17} In weak crystal fields, it was shown that multiple quantum coherence can be induced and controlled.^{18–20} In this paper, by means of incoherent (continuous wave) and coherent (pulsed wave) EPR, we describe the quantum dynamics of DMAMgF:Mn²⁺. We show how the complex quantum dynamics of Mn²⁺ in moderate crystal fields can be resolved using a kernel density estimation (Fig. 2).

II. MATERIALS AND METHODS

A. Sample preparation

DMAMgF:Mn²⁺ samples were prepared using the method similar to the one described in detail in our earlier paper with some minor modifications. A 23 ml solution of 50 vol. % dimethylformamide (DMF) in nanopure water, into which 85.0 mM MgCl₂ and 2 μ M MnCl₂ (0.002%) were dissolved, was sealed in a 35 ml pressure vessel. The pressure vessel was then heated to 140 °C for 2 days and then allowed to cool to room temperature (RT). Once cooled, the supernatant was decanted. Single crystals were obtained by slowly evaporating the solution in a 10 dram glass vial with 1 in. diameter. We assumed a cuboid shape of the crystal, and the axes of the Cartesian reference frame were chosen such that they coincide with the edges of the crystal.

B. Single crystal x-ray diffraction

A suitable crystal for the compound DMAMgF:Mn²⁺ was measured on a Rigaku Oxford Diffraction SuperNova diffractometer at 220 K ($< T_c = 260$ K) under Cu K α radiation ($\lambda = 1.54184$ Å). Data collection reduction and multiscan ABSPACK correction were performed with CrysAlisPro (Rigaku Oxford Diffraction). Using Olex2,²¹ the structures were solved by intrinsic phasing methods with SHELXT,²² and SHELXL²³ was used for full matrix least squares refinement. All H-atoms were found experimentally, and their coordinates and Uiso parameters were constrained to 1.5Ueq (parent atoms) for the methyl groups and to 1.2Ueq (parent atom) for the other carbon atoms.

C. EPR spectroscopy

X-band (about 9.6 GHz) EPR measurements were performed using two conventional Bruker spectrometers operating in the continuous wave (cw) mode X-band (EMX, 9.6 GHz) and pulse mode X-band (E680, 9.6 GHz). The cw spectrometer uses a standard 4102ST resonator (TE₁₀₂) installed in an Oxford cryostat ESR900. Low temperature measurements were performed using a cryogen-free Bruker Stinger cryocooler, allowing the temperature to reach 7 K. The angular dependence was measured using an automatic goniometer. Magnetic field modulation ($f_m = 100$ kHz) associated with lock-in detection was employed, resulting in the derivative of the signal. The amplitude of the modulation can be set up to 10 G and was

carefully chosen to be below any linewidth to avoid the overmodulation effect.

The pulse spectrometer was used to perform Rabi oscillation measurements on Mn^{2+} ions²⁰ using the sequence $P_R - \tau_1 - \pi/2 - \tau_2 - \pi - \text{echo}$, where P_R is the Rabi pulse that controls the coherent rotation of the spin and τ_1 is the wait time longer than the coherence time in order to destroy the transverse magnetization T_2 but shorter than the relaxation time T_1 maintaining the longitudinal magnetization $\langle S_z \rangle$. The latter is then recorded by the standard Hahn echo. Due to the large distribution of transitions, the $\pi/2$ pulse is selective in DMAMgF:Mn²⁺. However, it is more convenient in the field sweep Rabi oscillation sequence since one wants to excite just a small quantity of spins (the ones actually in resonance) in the spin packet. The measurements were performed at 7 K using the Bruker MD5 dielectric resonator overcoupled. The microwave field h_{mw} was calibrated by measuring the nutation of a $S = 1/2$ standard.

High-field/high-frequency EPR (HF-EPR) experiments have been carried out using a homemade quasioptical superheterodyne setup developed at the NHMFL.²⁴ The spectrometer operates at 240 GHz and at temperatures from RT down to 5 K. Angular dependence with respect to the magnetic field direction is achieved using a manual goniometer every 18°.

D. DFT

All theoretical calculations were based on Density Functional Theory (DFT) and were performed with the ORCA program package.²⁵ To facilitate comparisons between theory and experiments, all DFT models were obtained from the experimental x-ray crystal structures and were optimized while constraining the positions of all heavy atoms to their experimentally derived coordinates. Only the positions of the hydrogen atoms were relaxed because these are not reliably determined from the x-ray structure. Geometry optimizations were undertaken using the GGA functional BP86^{26–28} in combination with the TZVP²⁹ basis set for all atoms and by exploiting the resolution of the identity (RI) approximation in the Split-RI-J variant³⁰ with the appropriate Coulomb fitting sets.³¹ Increased integration grids (Grid4 and GridX4 in ORCA convention) and tight SCF convergence criteria were used. The zero-field splitting (ZFS) parameters were obtained from additional single-point calculations using the BP86 functional. Scalar relativistic effects were included using ZORA paired with the SARC def2-TZVP(-f) basis sets^{32,33} and the decontracted def2-TZVP/J Coulomb fitting basis sets for all atoms. The spin–spin contribution to the ZFS was calculated on the basis of the UNO determinant.³⁴

III. RABI DISTRIBUTION CALCULATION

To simulate the EPR spectra, we used the following Hamiltonian:

$$\mathcal{H} = \mu_b \vec{H} [g] \vec{S} + \vec{S} [A] \vec{I} + \sum_k \sum_q B_k^q \hat{O}_k^q(\vec{S}), \quad (1)$$

where the first term represents the Zeeman interaction with the g tensor $[g]$ and μ_b is the Bohr magneton, the second term represents the hyperfine interaction with the hyperfine tensor $[A]$ considered as isotropic, and the last term represents the crystal–field interaction in the formalism of the extended Stevens operators^{35,36} $\hat{O}_k^q(\vec{S})$ ($k = 2, 4, 6$ and $q = -k, \dots, k$). B_k^q are real coefficients with the

relations: $3B_2^0 = D$ is the axial anisotropy, $B_2^2 = E$ is the rhombic anisotropy, $24B_4^4 = a$ is the cubic contribution, and $F = 180B_4^0 - 36B_4^4$ is the fourth order contribution. $k = 6$ terms were considered small enough to be neglected. $[g]$ and $[A]$ are considered as scalar (isotropic) for Mn^{2+} .

The EPR simulations were performed using a hybrid method. The conventional cw EPR spectra were simulated using the MATLAB package EasySpin v5.2.28.³⁷

The Rabi mode distributions were computed using a database approach. Due to the large anisotropy and the disoriented nature of DMAMgF:Mn²⁺ at low temperatures, the full dynamical density matrix model developed in Ref. 38 for n photon transitions would have been too heavy to implement and unnecessary. Due to the large ZFS expected in this family of compounds,^{5,13} only the 1-photon transitions are expected to occur (n -photon transitions are expected when $D \sim h_{mw}$,³⁹ with h_{mw} as the microwave field). Using the first order Fermi's golden rule, the Rabi frequency of a transition m to n is $|\langle m | S^+ | n \rangle|$. The database of the Rabi frequencies was constructed as follows. The static field orientation is set first, and then, after diagonalization of the Hamiltonian, all transition fields are computed (regardless of the intensity), the Rabi frequency of each transition is calculated by Fermi's golden rule, and the intensity of the transition simply equals the square of the Rabi frequencies. Orientations, resonance fields, transitions, and Rabi frequencies are collected in the database. The treatment of the data is then realized using the Pandas module of Python 3.8. We use the kernel density estimation (KDE)⁴⁰ to reconstruct the Rabi oscillation distribution,

$$\hat{f}_h(x) = \frac{1}{n} \sum_{i=1}^n K_h(x - x_i), \quad (2)$$

where K is the kernel function, h is the bandwidth, and n is the number of samples. This method can be seen as an extension of the histogram method, which counts the number of occurrences around a value. In our analysis, we used the Gaussian kernel function. Since we have access to the transitions, field resonances, and orientations, we can identify the nature and distribution of all transitions.

IV. RESULTS AND DISCUSSION

A. HT phase

Continuous wave EPR studies have been previously reported for the LT phase of the Zn compound, DMAZnF:Mn²⁺,^{12,13} and a particular focus has been made on the dynamics in the HT phase.⁵ Here, we are interested in determining the focus on how the change from Zn to Mg, which highly affects the structural phase transition temperature, can also have effects on the dynamics probed by EPR. Figure 3(a) shows the EPR signal of DMAMgF:Mn²⁺ for H||[102] at room temperature. The signal is composed of six lines corresponding to the m_I nuclear spin projection of ⁵⁵Mn. The separation between lines is 93.6 G, which corresponds to 262.3 MHz or $87.5 \times 10^{-4} \text{ cm}^{-1}$ and is a classical value reported for Mn²⁺ ions.⁴¹ In solid-state EPR and for single crystal measurements, the intensity and linewidth of the six line pattern are expected to be comparable, while in our case, the lines at the lowest and highest fields (corresponding to $m_I = \pm 5/2$) are clearly sharper than the ones present in the intermediate field region. Moreover, no forbidden transition⁴² is resolved, while it is usually observed in

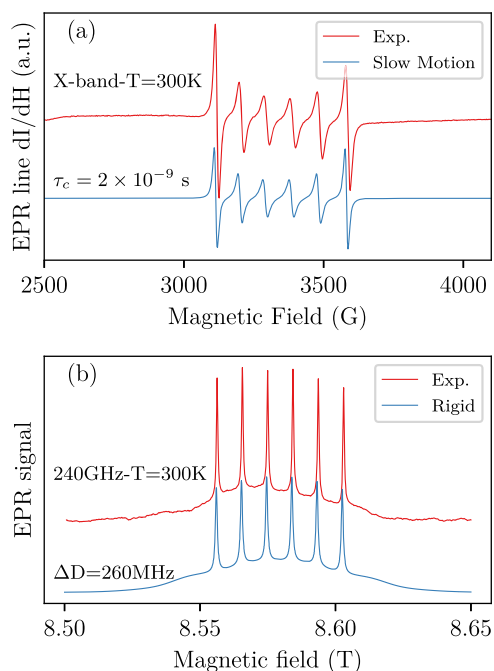


FIG. 3. (a) First derivative with respect to the field of the EPR signal of a single crystal of DMAMgF:Mn²⁺ recorded at the X-band and room temperature (red line). The blue line below represents the simulation of the spectrum in the slow motion regime with a correlation time $\tau_c = 2 \times 10^{-9}$ s. (b) EPR signal recorded on the same crystal at $f_{mw} = 240$ GHz and at room temperature. The blue line is the rigid limit spectrum simulation using a distribution of the axial anisotropy ΔD .

Mn²⁺ ions in the anisotropic crystal field. This behavior was also observed⁵ in DMAZnF:Mn²⁺ and was attributed to the slow motion regime^{43–45} caused by the DMA⁺ movement around the Mn²⁺ ion. Using this model,⁴³ we managed to simulate the experimental data within DMAZnF:Mn²⁺. Indeed, by decreasing the temperature, the DMA⁺ cations slow down, and when the correlation time τ_c is longer than the time scale of the measurement (i.e., $>1/f_{mw}$), the system is considered frozen and can be described by the rigid model. However, in DMAMgF:Mn²⁺, T_c (263 K) is higher than those in the Zn counterparts (173 K) and the structure of the system changes before reaching the frozen regime. To observe the frozen regime, we have to increase the frequency significantly. Figure 3(b) shows the EPR signal of DMAMgF:Mn²⁺ recorded at $f_{mw} = 240$ GHz and at room temperature. Contrary to the X-band measurements, all six nuclear isotope lines for the transition $m_S = -1/2 \leftrightarrow 1/2$ have the same intensity, suggesting that we have reached the rigid limit of EPR. However, whatever the orientation of the crystal is, no satellite lines corresponding to $m_S = \pm 5/2 \leftrightarrow \pm 3/2$ and $m_S = \pm 3/2 \leftrightarrow \pm 1/2$ were resolved, indicating a large distribution of the crystal field parameters. To simulate the spectrum of Fig. 3(b), we used the crystal field parameters of the DMAZnF:Mn²⁺ compound,⁵ $D = B_0^2/3 = 250$ MHz, but we have to set a distribution of the crystal field parameter $\Delta D = 260$ MHz, which seems inconsistent since ΔD is usually less than 10% of D . To explain this large value of ΔD , it is worth to mention that in the HT phase, the system is locally highly disordered. Indeed, the Mn²⁺ ion is surrounded by 8 DMA⁺ cations,

which have three different positions, giving rise to $3^8 = 6561$ configurations of the crystal field, which are responsible for the large ZFS distribution.

To support and rationalize the experimental findings about ΔD , DFT calculations were conducted. To do so, we employed a methodology similar to that from our previous study on DMAZnF:Mn²⁺⁴⁶ and worked with a minimal model consisting of one Mn²⁺ ion bound to 6 formate anions and surrounded by 8 DMA⁺ cations (see the supplementary material). The resulting metal cluster displays a quasi-octahedral coordination geometry. Based on the high temperature single crystal XRD structure of DMMgF that identified three equivalent positions of nitrogen in each DMA⁺ cation, we have considered several configurations in which the Mn–N distances for 6 DMA⁺ cations can take values of 4.495, 5.121, and 5.679 Å, while the two remaining DMA⁺ cations display Mn–N distances of 5.698 Å. This provides a random sampling of the different situations and allows us to determine the distribution of the ZFS parameter, which was found to be $\Delta D \approx 234$ MHz. The computed value is in fair agreement with the experimentally estimated value of 260 MHz, and our calculations adequately reproduce the increased value for the ZFS distribution when comparing DMAMgF:Mn²⁺ to DMAZnF:Mn²⁺ ($\Delta D_{DFT} \approx 125$ MHz and $\Delta D_{exp} \approx 150$ MHz, respectively). While there is no clear evidence for an effect from Mg, our results confirm the influence from the DMA⁺ cations on the crystal-field effect on Mn²⁺ as observed in the case of DMAZnF:Mn²⁺.

Figure 4 shows the temperature dependence of the peak-to-peak linewidth ΔH_{pp} of the smallest field line ($m_I = -5/2$) for DMAMgF:Mn²⁺ (this work) and DMAZnF:Mn²⁺ (from Ref. 5) in the HT phase. In DMAZnF:Mn²⁺, $T_c = 170$ K, while in DMAMgF:Mn²⁺, $T_c = 260$ K so that the temperature range of the HT phase in DMAMgF:Mn²⁺ is more limited. In the X-band and in the slow regime, the temperature dependence of ΔH_{pp} is barely the same in the two compounds, showing that the correlation time τ_c of the DMA⁺ cation is weakly affected by the nature of the metal, Zn or Mg, as pointed out in Ref. 47. In the rigid limit, the linewidth of the $m_S = -1/2 \leftrightarrow 1/2$ transition in DMAMgF:Mn²⁺ is about two times smaller than that in DMAZnF:Mn²⁺ at high frequencies although the working frequency used to investigate DMAMgF:Mn²⁺ was 240 GHz, while it was 34 GHz for DMAZnF:Mn²⁺. The distribution

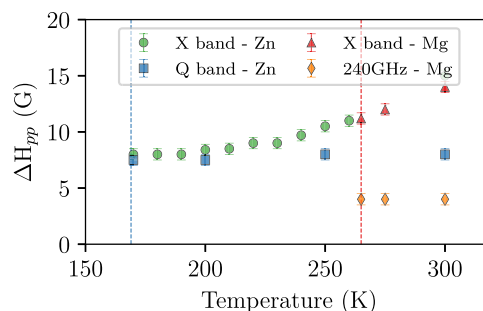


FIG. 4. Peak-to-peak linewidth of the rightmost EPR line in DMAMgF:Mn²⁺, recorded between 300 and 260 K at the X-band and 240 GHz. The data for DMAZnF:Mn²⁺ were extracted from Ref. 5. The vertical dashed line is the structural transition temperature.

of the crystal field does not affect this transition, and the distribution of the g -factor should have an effect to increase the linewidth when the frequency is increased.

B. LT phase

1. CW-EPR

When the temperature is below $T_c = 263$ K, the system undergoes a structural phase transition from disordered trigonal $R\bar{3}c$ to ordered monoclinic Cc . Figure 5 shows the EPR spectrum of DMAMgF:Mn²⁺ powder at $T = 100$ K. The signal is now more resolved than that in the HT phase due to an apparent decrease in the ΔD value. Using Eq. (1), we simulated the spectrum with the following parameters: $B_2^0 = 110$ MHz, $B_2^2 = 10$ MHz, $B_4^0 = 0.5$ MHz, $B_4^2 = 0.7$ MHz, $B_4^4 = 0.5$ MHz, and $A = 264$ MHz. While the second order crystal field parameters are provided with a good approximation, the fourth order ones have to be taken with caution since the transitions $m_S = \pm 5/2 \leftrightarrow \pm 3/2$ and $m_S = \pm 3/2 \leftrightarrow \pm 1/2$ are not perfectly resolved. Nevertheless, the crystal field parameters are in the range of what is expected for this family of materials.¹³ The crystal field distribution ΔD is about 50 MHz, which is much less than the one needed to simulate the HT phase. In the LT phase, the DMA⁺ cations now have only one possible orientation induced by the ferroelastic phase. The residual ΔD is thus due to local inhomogeneity.

Figure 6 shows the angular dependence of the X-band EPR signal of DMAMgF:Mn²⁺ recorded at $T = 100$ K with a resolution of 1° in the relative orientation. The rotation was performed around the [012] axis. Most of the transitions are between 3000 and 3500 G and are therefore impossible to resolve. However, the highest anisotropic transitions, $m_S = \pm 5/2 \leftrightarrow \pm 3/2$, are visible on the edges of the spectra. The triangles point to the maximum of the resonance fields and are found at 18° and 108° for the blue ones and at 55° and 145° for the red ones. The angular separation between these two magnetic inequivalent sites is 53°, which corresponds to the angle between the two MnO₆ orientations resolved by XRD (see Fig. S1 of the supplementary material). It is worth noticing that in DMAZnF:Mn²⁺, six substructures were necessary to describe the angular dependence of the EPR.¹⁵ Single crystal XRD data obtained at 100 K reveal the presence of a two component twin with a minor domain of only 5% weight (see Fig. S2 of the supplementary material).

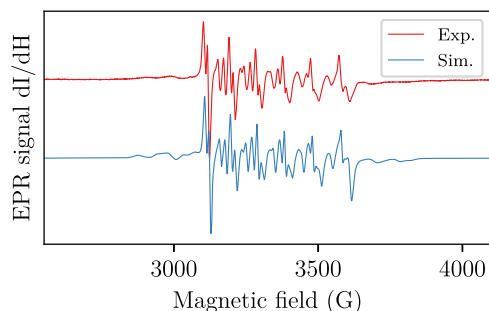


FIG. 5. First derivative of the EPR spectrum of DMAMgF:Mn²⁺ recorded on a powder sample at $T = 100$ K and $f_{mw} = 9.6$ GHz (red line). The best simulation obtained using the parameters reported in the main text is presented in blue.

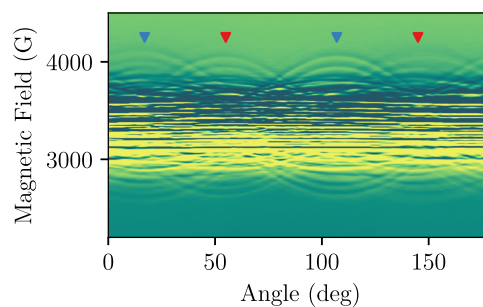


FIG. 6. Angular dependence of the EPR signal of a single crystal of DMAMgF:Mn²⁺ recorded at $T = 100$ K and $f_{mw} = 9.6$ GHz. Rotation was performed around the [012] axis. The blue and red triangles show the extreme resonance field of the $m_S = \pm 5/2 \leftrightarrow \pm 3/2$ transitions (the only well-resolved field) and help identify the two magnetic structures.

To confirm that DMAMgF:Mn²⁺ has mostly a single ferroelastic domain, we performed high frequency/field EPR (240 GHz ≈ 8.87 T) at $T = 5$ K. At this temperature and for this field, the Boltzmann statistic populates mostly the lowest energy levels ($m_S = -5/2$). The transitions $m_S = -5/2 \leftrightarrow -3/2$ are mainly visible, while the others are either weak or absent. Thus, the spectra are “cleaned” and easier to read. Figure 7 shows the angular dependence of DMAMgF:Mn²⁺ at $f = 240$ GHz. Blue and red triangles represent the resonance fields and are useful to follow the angular variation of the resonance fields of the two magnetic inequivalent sites. The blue and red lines are simulated using the crystal field parameters extracted from X-band measurements. The high field EPR data show that the field has no effect on the line separation due to the crystal field and hyperfine interaction. Consequently, the crystal field parameters remain identical to those obtained from X-band data. However, the g factor can be highly refined, and we used $g = 1.9985$ in our simulations. We can clearly distinguish the two inequivalent magnetic systems. The small signals at 90° and 108° are due to the thermal population of the $m_S = -3/2$ state, which is caused by the temperature instability in the cryostat.

While EPR studies¹⁴ have clearly shown the presence of three crystallographic twins of two magnetic domains in DMAZnF:Mn²⁺, we observe only a single domain of the two magnetic structures. If one considers that changing the metal ion in DMAZF from Zn to Mg modifies the elastic property of the MOF, the same argument can be used to explain the dramatic increase in T_c in DMAMgF compared to DMAZnF.

2. Pulsed EPR

Despite our efforts to resolve all EPR lines in DMAMgF:Mn²⁺ using low and high frequency EPRs, the large number of lines in Mn²⁺ makes it difficult to identify them completely. By means of pulsed EPR, we measured the field sweep Rabi oscillations. Rabi spectroscopy adds another dimension to the EPR spectrum. While for a fixed field, the EPR intensity might contain many transitions with unresolved contribution, the Rabi frequency of each transition is often unique. In Fig. 8(a), we show the 1D echo field, and in Fig. 8(b), we show the contour plot of the field sweep Fast Fourier Transform (FFT) of Rabi oscillations recorded on a single crystal of DMAMgF:Mn²⁺ at $T = 7$ K with $h_{mw} = 4.8$ G. The red dashed line

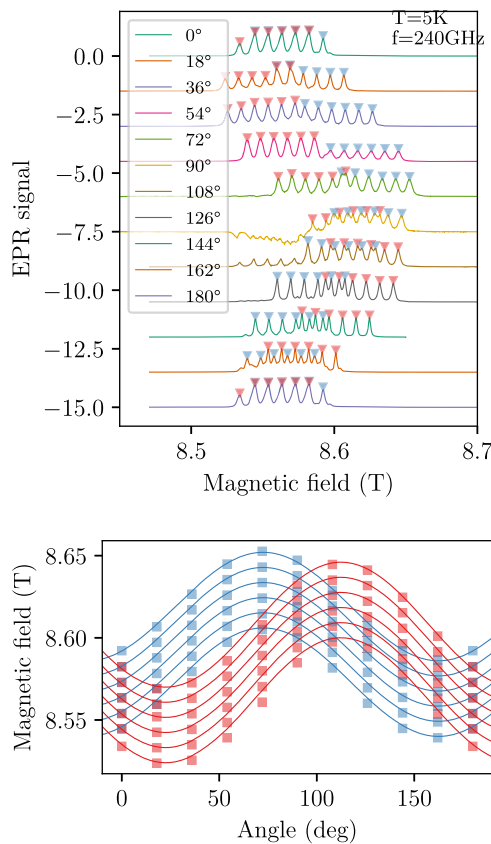


FIG. 7. (Top) Angular dependence of the HF-EPR spectra of a single crystal of DMAMgF:Mn²⁺ recorded at $T = 5$ K. Rotation was performed around the [012] axis. Blue and red triangles indicate the resonance field. Temperature stability was not perfect, and satellite lines from $m_S = -3/2 \leftrightarrow -1/2$ can be seen at 90° and 108° . (Bottom) Angular dependence of the resonance fields. The squares represent the resonance fields, and the lines correspond to the simulations of the resonance field using Eq. (1).

corresponds to the frequency expected for a $S = 1/2$ spin. Clearly, the 2D Rabi field sweep helps resolve many more transitions. The distribution in the frequency dimension is due to the damping of the oscillation, while the distribution in the field dimension is due to ΔD . Qualitatively, the broadly distributed frequencies are related to the $m_S = \pm 5/2 \leftrightarrow \pm 3/2$ and $m_S = \pm 3/2 \leftrightarrow \pm 1/2$ transitions, which are sensitive to ΔD , while the narrow distributed ones are related to $m_S = -1/2 \leftrightarrow \pm 1/2$, which are insensitive to the crystal field. Moreover, in the first approximation, the Rabi frequency in a large spin system is given by the adapted Fermi's golden rules,⁴⁸

$$F_R(S, m_S) = \sqrt{S(S+1) - m_S(m_S+1)} \times F_R(S = 1/2), \quad (3)$$

such as $F_R(S = 5/2, m_S = -5/2) = \sqrt{5} \times F_R(S = 1/2) = 30.2$ MHz, $F_R(S = 5/2, m_S = -3/2) = \sqrt{8} \times F_R(S = 1/2) = 38.8$ MHz, and $F_R(S = 5/2, m_S = -1/2) = \sqrt{9} \times F_R(S = 1/2) = 40.5$ MHz.

While the agreement with this model is fair (but not exact) for $m_S = \pm 5/2 \leftrightarrow \pm 3/2$ and $m_S = \pm 3/2 \leftrightarrow \pm 1/2$, it fails for $m_S = -1/2 \leftrightarrow +1/2$. To understand the distribution of Rabi frequencies in

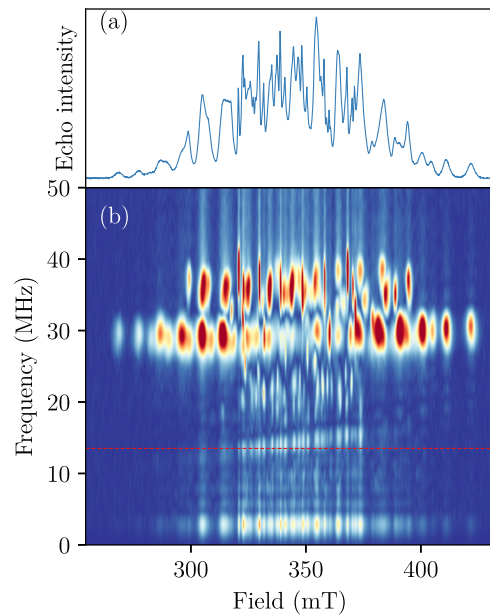


FIG. 8. (a) Echo field sweep of a single crystal of DMAMgF:Mn²⁺ at $T = 7$ K. (b) Fast Fourier transform of the field sweep Rabi oscillations for the same orientation with a pumping pulse of strength $h_{mw} = 4.8$ G. Red (blue) regions denote the presence (absence) of frequency density. The red dashed line represents the frequency expected for $S = 1/2$ at the same pulse amplitude.

DMAMgF:Mn²⁺, we developed a kernel density estimation of all transitions and all orientations in the crystals. Using the crystal field parameters found in Sec. IV B 1, we computed the fields of resonance for each (allowed and forbidden) transition accessible from $H = 260$ mT to $H = 430$ mT. For each pair of resonance field/transition, we computed the amplitude of transition probability (A_{tr}) in the direction perpendicular to the field orientation that is imposed by the experimental condition since the cavity forces the microwave polarization to be perpendicular to the static field. The Rabi frequency is then $F_R = \frac{g\mu_b h_{mw}}{h} A_{tr}$, with g as the g-factor (close to 2), μ_b as the Bohr magneton, h as the Planck constant, and h_{mw} as the microwave field. This series of Rabi frequencies is then computed for all orientations. We discretize the space using an icosphere to avoid over-density of orientations by using a simple set of equally spaced Euler's angles. The calculation included 20 609 orientations, and using a threshold of 10^{-2} to suppress the far too low frequency Rabi oscillations, we obtained 1 346 898 sets of data containing resonance fields, probability amplitude, transition identification, and Euler angles.

We first describe the Rabi frequency and field distribution for the “allowed” transitions ($\Delta m_S = \pm 1$ and $\Delta m_I = 0$). Figure 9 shows the Rabi frequencies and magnetic field distributions for the 30 allowed transitions. First, the field distribution follows what we expected for a Mn²⁺ ion in a moderate crystal field: $m_S = \pm 5/2 \leftrightarrow \pm 3/2$ transitions are spread on a large distribution of the field and $m_S = \pm 3/2 \leftrightarrow \pm 1/2$ transitions are slightly less distributed, while $m_S = -1/2 \leftrightarrow +1/2$ transitions are fairly insensitive to the crystal field and induce the narrow lines observed in Fig. 8. More

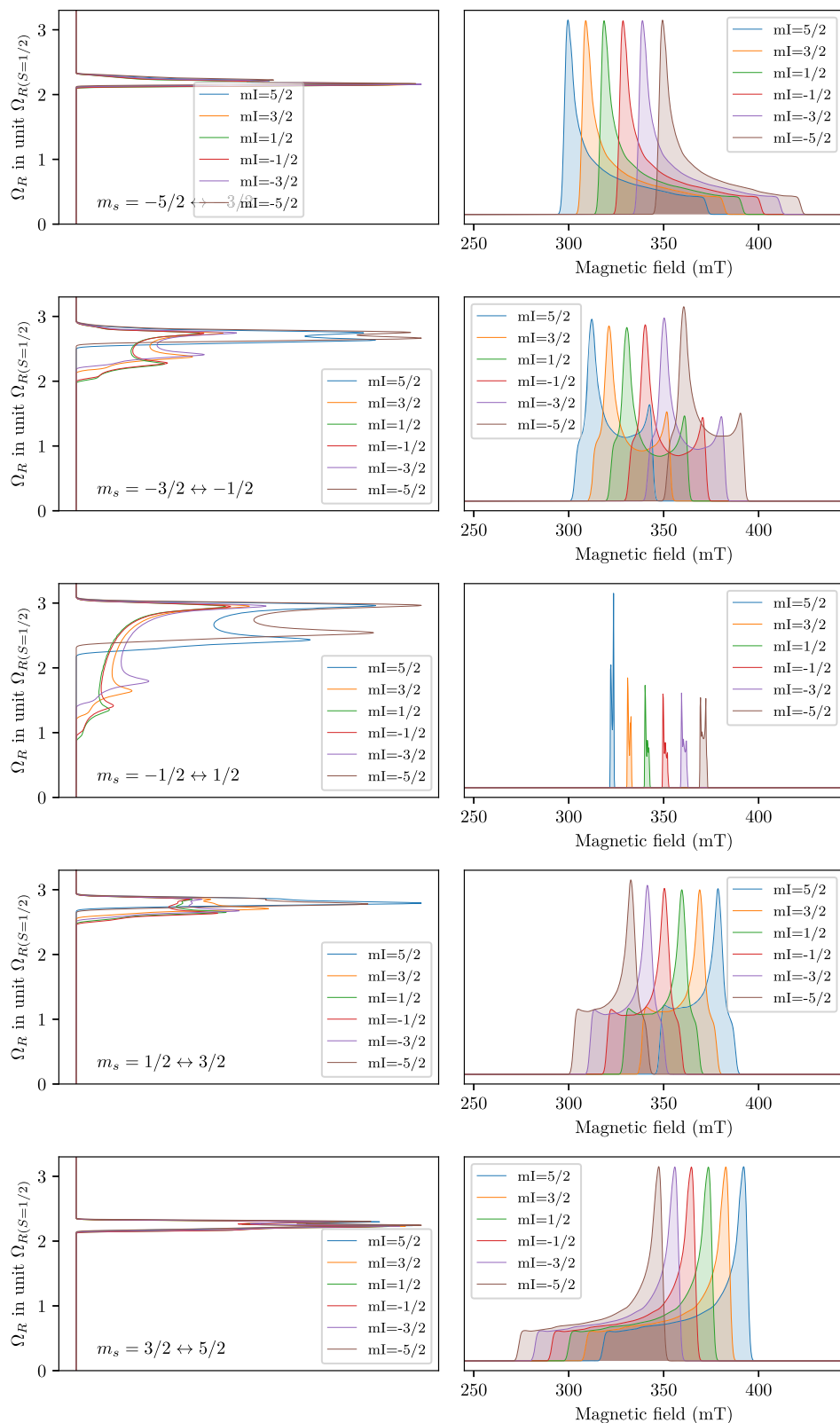


FIG. 9. Rabi frequency (left) and resonance field (right) distributions calculated in DMAMgF:Mn²⁺ using the crystal field parameters extracted from CW measurements for all allowed transitions ($\Delta m_S = \pm 1$ and $\Delta m_I = 0$). The frequency distribution is presented vertically to help in the comparison with the experimental data. The unit is set to be proportional to the Rabi frequency of the $S = 1/2$ isotropic calibrator.

surprisingly, the Rabi frequency distribution is less intuitive. The transitions $m_S = \pm 5/2 \leftrightarrow \pm 3/2$ are weakly distributed around $2.2 \times F_R(S = 1/2)$ whatever m_I is, confirming the validity of Eq. (3), while the $m_S = \pm 3/2 \leftrightarrow \pm 1/2$ transitions are different. $m_I = \pm 5/2$ transitions also show a weak frequency distribution around $2.8 \times F_R(S = 1/2)$, but the transitions $m_I = \pm 3/2$ and $m_I = \pm 1/2$ are much more distributed. The transitions $m_S = -1/2 \leftrightarrow +1/2$ are even more sensitive to the orientation. In this case, the Rabi frequency distribution is very broad and dependent on the m_I value, while the resonance field distribution is essentially independent of the orientation. This explains why the $m_S = -1/2 \leftrightarrow +1/2$ transition is narrow in the field dimension but distributed in a large range of Rabi frequencies (see Fig. 8).

Now, we consider the case of Rabi frequencies and resonant field distributions of the “forbidden” transitions. The calculation method is based on the first order Fermi’s golden rule, and so only one photon is involved in the resonance mechanism. The multiple photon transitions^{18,19,49} $\Delta m_S > 1$ are not taken into account. However, such transitions are induced only when $h_{mw} \sim D$, which is far from being the case here. The “forbidden” transitions that we consider are thus $\Delta m_S = \pm 1$ and $\Delta m_I \neq 0$. It appears that the transitions $m_S = -1/2 \leftrightarrow 1/2$ and $m_I = -1/2 \leftrightarrow 1/2$ (see the [supplementary material](#)) are weakly distributed in the field, which is expected for such transitions, but we also observe that the Rabi frequency distribution is centered at $1.6 \times F_R(S = 1/2)$, making these transitions highly probable.

To confront the model, we have measured the field sweep Rabi oscillations of a powder of DMAMgF:Mn²⁺. After some signal processing (baseline correction, hamming, and zero filing), the FFT is presented in Fig. 10(a). We then simulated the distribution of both frequencies and resonance fields of a Mn²⁺ ion with the crystal field parameters extracted from the CW-EPR of DMAMgF:Mn²⁺ and a microwave field of $h_{mw} = 1.8$ G. Our simulation describes the experimental data rather well. We should note that the apparent slope in the Rabi frequencies around 15 MHz in Fig. 10(a) is due to the nuclear Zeeman interaction from protons ω_N (42.57 MHz/T) that induce an amplification of the Rabi intensity in the case of Hartman–Hahn conditions⁵⁰ ($\omega_N \sim \Omega_R$). Without fitting parameters, we can describe the experimental data, but the strength of this method is to help in the identification of transitions. Figures S6 and S7 show the frequency and field distribution of all principal transitions.

To simulate the single crystal field sweep Rabi frequency distribution presented in Fig. 8, we just replaced the Euler angle sweep by the distribution of the crystal field parameter D in order to simulate the broadening. We used a Gaussian distribution with a width of 40 MHz corresponding to the D -strain extracted from EPR measurements. We then calculated the field sweep Rabi frequency distribution for two orientations separated by 58°, which correspond to the angle between the two magnetic domains observed in Fig. 6 and is presented in Fig. S8. The agreement between theory and experiment (Fig. 8) is fairly good, thus confirming the presence of two magnetic structures that are disoriented by about 60°. We also note that very low modes at about 2.5 MHz are visible experimentally but not displayed in our model. We believe these modes are related to the recently observed quantum rotor tunneling of the methyl group in DMAZnF,⁵¹ which has not been taken into account in our model.

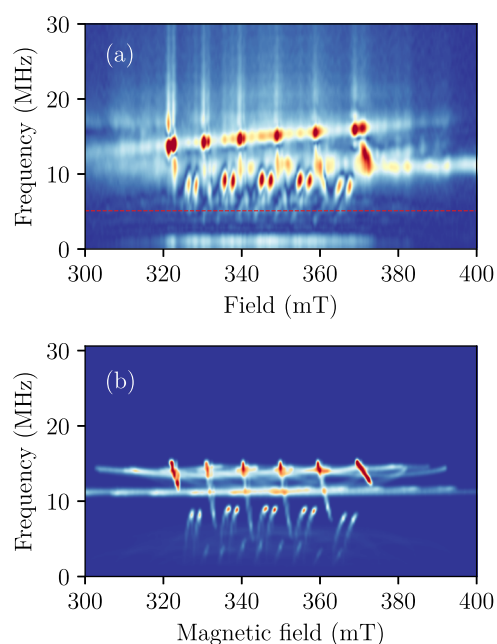


FIG. 10. (a) Fast Fourier transform of the field sweep Rabi oscillations for a powder sample of DMAMgF:Mn²⁺. A pumping pulse of strength $h_{mw} = 1.8$ G was used. Red (blue) regions denote the presence (absence) of frequency density. The red dashed line represents the frequency expected for $S = 1/2$ at the same pulse amplitude. (b) Simulation of Rabi oscillations in a powder using the crystal field parameters of DMAMgF:Mn²⁺.

V. CONCLUSION

We employed the electron spin resonance technique to investigate the dynamics of the electron spin of a Mn²⁺ ion used as a probe in the DMAMgF compound. In the high temperature phase, the X-band cw-EPR study demonstrated that the correlation time describing the motion of DMA⁺ cations in DMAMgF:Mn²⁺ is similar to that observed in the Zn analog. The high frequency EPR data revealed a large ZFS distribution in DMAMgF:Mn²⁺. Using a wide range of configurations and DFT computations, we were able to support this finding and fairly estimate this distribution. In the low temperature phase, we observed a single elastic phase containing two magnetic structures in agreement with single crystal XRD analysis. The complex EPR structure observed in the LT phase was then solved using pulsed EPR combined with the field sweep Rabi oscillation method. A model based on the crystal field and the kernel density estimation of all possible transitions and orientations finally provided an accurate description of the complicated EPR structure of DMAMgF:Mn²⁺.

SUPPLEMENTARY MATERIAL

See the [supplementary material](#) for the XRD data and structure description, details about DFT minimal models, and simulation of Rabi field sweep distributions.

AUTHORS' CONTRIBUTIONS

S.B. and N.D. designed and directed the study. J.K.B. synthesized the samples. J.K.B. and J.v.T. conducted the HF-EPR measurements. S.B. performed the X-band EPR measurements. M.G. performed the XRD measurements. M.O. carried out the DFT calculations. M.O. and S.B. conducted the theoretical analysis and wrote the paper with input from all authors. All authors contributed to the implementation of the research and to the analysis of the results.

ACKNOWLEDGMENTS

Pulsed ESR measurements were supported by the Centre National de la Recherche Scientifique (CNRS) research infrastructure RENARD (Grant No. IR-RPE CNRS 3443). We acknowledge the international research program of CNRS PICS SomeTIME. The NHMFL is supported by the NSF Cooperative Agreement (Grant No. DMR-1157490) and the State of Florida.

DATA AVAILABILITY

The data that support the findings of this study are openly available in Zenodo at <http://doi.org/10.5281/zenodo.4521882>.

REFERENCES

- P. Jain, N. S. Dalal, B. H. Toby, H. W. Kroto, and A. K. Cheetham, "Order-disorder antiferroelectric phase transition in a hybrid inorganic-organic framework with the perovskite architecture," *J. Am. Chem. Soc.* **130**, 10450–10451 (2008).
- T. Besara, P. Jain, N. S. Dalal, P. L. Kuhns, A. P. Reyes, H. W. Kroto, and A. K. Cheetham, "Mechanism of the order-disorder phase transition, and glassy behavior in the metal-organic framework $[(\text{CH}_3)_2\text{NH}_2]\text{Zn}(\text{HCOO})_3$," *Proc. Natl. Acad. Sci. U. S. A.* **108**, 6828–6832 (2011).
- P. Jain, V. Ramachandran, R. J. Clark, H. D. Zhou, B. H. Toby, N. S. Dalal, H. W. Kroto, and A. K. Cheetham, "Multiferroic behavior associated with an order-disorder hydrogen bonding transition in metal-organic frameworks (MOFs) with the perovskite ABX_3 architecture," *J. Am. Chem. Soc.* **131**, 13625–13627 (2009).
- N. Abhyankar, S. Bertaina, and N. S. Dalal, "On Mn^{2+} EPR probing of the ferroelectric transition and absence of magnetoelectric coupling in dimethylammonium manganese formate $(\text{CH}_3)_2\text{NH}_2\text{Mn}(\text{HCOO})_3$, a metal-organic complex with the Pb-free perovskite framework," *J. Phys. Chem. C* **119**, 28143–28147 (2015).
- S. Bertaina, N. Abhyankar, M. Orio, and N. S. Dalal, "Measuring motional dynamics of $[(\text{CH}_3)_2\text{NH}_2]^+$ in the perovskite-like metal-organic framework $[(\text{CH}_3)_2\text{NH}_2][\text{Zn}(\text{HCOO})_3]$: The value of low-frequency electron paramagnetic resonance," *J. Phys. Chem. C* **122**, 16431–16436 (2018).
- Z. Wang, P. Jain, K. Y. Choi, J. Van Tol, A. K. Cheetham, H. W. Kroto, H. J. Koo, H. Zhou, J. Hwang, E. S. Choi, M. H. Whangbo, and N. S. Dalal, "Dimethylammonium copper formate $[(\text{CH}_3)_2\text{NH}_2]\text{Cu}(\text{HCOO})_3$: A metal-organic framework with quasi-one-dimensional antiferromagnetism and magnetostriction," *Phys. Rev. B* **87**, 224406 (2013).
- M. Sánchez-Andújar, L. C. Gómez-Aguirre, B. Pato Doldán, S. Yáñez-Vilar, R. Artiaga, A. L. Llamas-Saiz, R. S. Manna, F. Schnelle, M. Lang, F. Ritter, A. A. Haghghirad, and M. A. Señaris-Rodríguez, "First-order structural transition in the multiferroic perovskite-like formate $[(\text{CH}_3)_2\text{NH}_2][\text{Mn}(\text{HCOO})_3]$," *CrystEngComm* **16**, 3558 (2014).
- B. Pato-Doldán, M. Sánchez-Andújar, L. C. Gómez-Aguirre, S. Yáñez-Vilar, J. López-Beceiro, C. Gracia-Fernández, A. A. Haghghirad, F. Ritter, S. Castro-García, and M. A. Señaris-Rodríguez, "Near room temperature dielectric transition in the perovskite formate framework $[(\text{CH}_3)_2\text{NH}_2][\text{Mg}(\text{HCOO})_3]$," *Phys. Chem. Chem. Phys.* **14**, 8498 (2012).
- T. Asaji, S. Yoshitake, Y. Ito, and H. Fujimori, "Phase transition and cationic motion in the perovskite formate framework $[(\text{CH}_3)_2\text{NH}_2][\text{Mg}(\text{HCOO})_3]$," *J. Mol. Struct.* **1076**, 719–723 (2014).
- M. Szafranski, W.-J. Wei, Z.-M. Wang, W. Li, and A. Katrusiak, "Research update: Tricritical point and large caloric effect in a hybrid organic-inorganic perovskite," *APL Mater.* **6**, 100701 (2018).
- N. Abhyankar, S. Bertaina, M. Orio, and N. S. Dalal, "Magnetic resonance probing of ferroelectricity and magnetism in metal-organic frameworks," *Ferroelectrics* **534**, 11–18 (2018).
- M. Šimėnas, A. Ciupa, M. Maćzka, A. Pöpl, and J. Banys, "EPR study of structural phase transition in manganese-doped $[(\text{CH}_3)_2\text{NH}_2][\text{Zn}(\text{HCOO})_3]$ metal-organic framework," *J. Phys. Chem. C* **119**, 24522–24528 (2015).
- M. Šimėnas, M. Ptak, A. H. Khan, L. Dagys, V. Balevičius, M. Bertmer, G. Völkel, M. Maćzka, A. Pöpl, and J. Banys, "Spectroscopic study of $[(\text{CH}_3)_2\text{NH}_2][\text{Zn}(\text{HCOO})_3]$ hybrid perovskite containing different nitrogen isotopes," *J. Phys. Chem. C* **122**, 10284–10292 (2018).
- M. Šimėnas, A. Kultaeva, S. Balčiūnas, M. Trzebiatowska, D. Klose, G. Jeschke, M. Maćzka, J. Banys, and A. Pöpl, "Single crystal electron paramagnetic resonance of dimethylammonium and ammonium hybrid formate frameworks: Influence of external electric field," *J. Phys. Chem. C* **121**, 16533–16540 (2017).
- M. Šimėnas, S. Balčiūnas, M. Trzebiatowska, M. Ptak, M. Mączka, G. Völkel, A. Pöpl, and J. Banys, "Electron paramagnetic resonance and electric characterization of a $[(\text{CH}_3)_2\text{NH}_2][\text{Zn}(\text{HCOO})_3]$ perovskite metal formate framework," *J. Mater. Chem. C* **5**, 4526–4536 (2017).
- D. Loss and D. P. DiVincenzo, "Quantum computation with quantum dots," *Phys. Rev. A* **57**, 120–126 (1998).
- M. N. Leuenberger and D. Loss, "Quantum computing in molecular magnets," *Nature* **410**, 789–793 (2001).
- S. Bertaina, L. Chen, N. Groll, J. Van Tol, N. S. Dalal, and I. Chiorescu, "Multiphoton coherent manipulation in large-spin qubits," *Phys. Rev. Lett.* **102**, 050501–050504 (2009).
- S. Bertaina, M. Martens, M. Egels, D. Barakel, and I. Chiorescu, "Resonant single-photon and multiphoton coherent transitions in a detuned regime," *Phys. Rev. B* **92**, 024408 (2015).
- S. Bertaina, N. Groll, L. Chen, and I. Chiorescu, "Multi-photon Rabi oscillations in high spin paramagnetic impurity," *J. Phys.: Conf. Ser.* **324**, 012008 (2011).
- O. V. Dolomanov, L. J. Bourhis, R. J. Gildea, J. A. K. Howard, and H. Puschmann, "OLEX2: A complete structure solution, refinement and analysis program," *J. Appl. Crystallogr.* **42**, 339–341 (2009).
- G. M. Sheldrick, "SHELXT—Integrated space-group and crystal-structure determination," *Acta Crystallogr., Sect. A: Found. Adv.* **71**, 3–8 (2015).
- G. M. Sheldrick, "Crystal structure refinement with SHELXL," *Acta Crystallogr., Sect. C: Struct. Chem.* **71**, 3–8 (2015).
- J. van Tol, L.-C. Brunel, and R. J. Wylde, "A quasioptical transient electron spin resonance spectrometer operating at 120 and 240 GHz," *Rev. Sci. Instrum.* **76**, 074101 (2005).
- F. Neese, "Software update: The ORCA program system, version 4.0," *Wiley Interdiscip. Rev.: Comput. Mol. Sci.* **8**, e1327 (2018).
- J. P. Perdew, "Density-functional approximation for the correlation energy of the inhomogeneous electron gas," *Phys. Rev. B* **33**, 8822–8824 (1986).
- J. P. Perdew, "Erratum: Density-functional approximation for the correlation energy of the inhomogeneous electron gas," *Phys. Rev. B* **34**(10), 7406 (1986).
- A. D. Becke, "Density-functional exchange-energy approximation with correct asymptotic behavior," *Phys. Rev. A* **38**, 3098–3100 (1988).
- A. Schäfer, C. Huber, and R. Ahlrichs, "Fully optimized contracted Gaussian basis sets of triple zeta valence quality for atoms Li to Kr," *J. Chem. Phys.* **100**, 5829–5835 (1994).
- F. Neese, "Metal and ligand hyperfine couplings in transition metal complexes: The effect of spin-orbit coupling as studied by coupled perturbed Kohn-Sham theory," *J. Chem. Phys.* **118**, 3939–3948 (2003).
- F. Weigend, "Accurate Coulomb-fitting basis sets for H to Rn," *Phys. Chem. Chem. Phys.* **8**, 1057 (2006).
- D. A. Pantazis, X.-Y. Chen, C. R. Landis, and F. Neese, "All-electron scalar relativistic basis sets for third-row transition metal atoms," *J. Chem. Theory Comput.* **4**, 908–919 (2008).

- ³³D. A. Pantazis and F. Neese, "All-electron scalar relativistic basis sets for the lanthanides," *J. Chem. Theory Comput.* **5**, 2229–2238 (2009).
- ³⁴S. Sinnecker and F. Neese, "Spin-spin contributions to the zero-field splitting tensor in organic triplets, carbenes and biradicals—A density functional and *ab initio* study," *J. Phys. Chem. A* **110**, 12267–12275 (2006).
- ³⁵A. Abragam, "Paramagnetic resonance and hyperfine structure in the iron transition group," *Phys. Rev.* **79**, 534 (1950).
- ³⁶I. D. Ryabov, "On the generation of operator equivalents and the calculation of their matrix elements," *J. Magn. Reson.* **140**, 141–145 (1999).
- ³⁷S. Stoll and A. Schweiger, "EasySpin, a comprehensive software package for spectral simulation and analysis in EPR," *J. Magn. Reson.* **178**, 42–55 (2006).
- ³⁸S. Bertaina, C.-E. Dutoit, J. Van Tol, M. Dressel, B. Barbara, and A. Stepanov, "Quantum coherence of strongly correlated defects in spin chains," *Phys. Procedia* **75**, 23–28 (2015).
- ³⁹S. Bertaina, N. Groll, L. Chen, and I. Chiorescu, "Tunable multiphoton Rabi oscillations in an electronic spin system," *Phys. Rev. B* **84**, 134433 (2011).
- ⁴⁰M. Rosenblatt, "Remarks on some nonparametric estimates of a density function," *Ann. Math. Stat.* **27**, 832–837 (1956).
- ⁴¹W. Low, "Paramagnetic resonance spectrum of manganese in cubic MgO and CaF₂," *Phys. Rev.* **105**, 793–800 (1957).
- ⁴²S. R. P. Smith, P. V. Auzins, and J. E. Wertz, "Angular dependence of the intensities of 'forbidden' transitions of Mn²⁺ in MgO," *Phys. Rev.* **166**, 222–225 (1968).
- ⁴³A. D. McLachlan, "Line widths of electron resonance spectra in solution," *Proc. R. Soc. A* **280**, 271–288 (1964).
- ⁴⁴E. Goldammer and H. Zorn, "Electron-paramagnetic-resonance study of manganese ions bound to concanavalin A," *Eur. J. Biochem.* **44**, 195–199 (1974).
- ⁴⁵E. von Goldammer, A. Muller, and B. E. Conway, "Electron paramagnetic relaxation and EPR-line shapes of manganese ions in a sulfonated polystyrene ion-exchange resin at various degrees of hydration," *Ber. Bunsengesellschaft Phys. Chem.* **78**, 35–42 (1974).
- ⁴⁶S. Bertaina, S. Gambarelli, T. Mitra, B. Tsukerblat, A. Müller, and B. Barbara, "Quantum oscillations in a molecular magnet," *Nature* **453**, 203–206 (2008).
- ⁴⁷S. K. Ramakrishna, K. Kundu, J. K. Bindra, S. A. Locicero, D. R. Talham, A. P. Reyes, R. Fu, and N. S. Dalal, "Probing the dielectric transition and molecular dynamics in the metal–organic framework [(CH₃)₂NH₂]Mg(HCOO)₃ using high resolution NMR," *J. Phys. Chem. C* **125**, 3441–3450 (2021).
- ⁴⁸A. Schweiger and G. Jeschke, *Principles of Pulse Electron Paramagnetic Resonance* (Oxford University Press, 2001).
- ⁴⁹P. P. Sorokin, I. L. Gelles, and W. V. Smith, "Multiple quantum transitions in paramagnetic resonance," *Phys. Rev.* **112**, 1513–1515 (1958).
- ⁵⁰S. R. Hartmann and E. L. Hahn, "Nuclear double resonance in the rotating frame," *Phys. Rev.* **128**, 2042–2053 (1962).
- ⁵¹M. Šimėnas, D. Klose, M. Ptak, K. Aidas, M. Maćzka, J. Banys, A. Pöpl, and G. Jeschke, "Magnetic excitation and readout of methyl group tunnel coherence," *Sci. Adv.* **6**, eaba1517 (2020).